

Cryo electron microscopy: 3-D reconstruction of stochastic objects having statistics with geometric symmetry from 2-D noisy conditionally-linear imaging

Nan Xu, *Student Member* and Peter C. Doerschuk, *Senior Member*

Abstract—The images obtained from cryo electron microscopy are the projection of many heterogeneous instances of the object under study (e.g., a virus). When the object is heterogeneous but has an overall geometric symmetry, it is natural to describe the object as stochastic with symmetrical statistics. A maximum likelihood reconstruction approach is described in which all instances of the object lack symmetry but the statistics of the ensemble of objects are constrained to have symmetry. This algorithm is demonstrated on bacteriophage HK97 and is contrasted with existing algorithms in which each object, while still heterogeneous, has the symmetry. Reconstruction results show that the proposed algorithm eliminates long-standing distortions in previous heterogeneity calculations associated with symmetry axes, and provides estimates that make more biological sense than the estimates of existing algorithms.

Index Terms—cryo electron microscopy, virus structural biology, 3-D signal reconstruction from projections, maximum likelihood estimation, random signal with symmetrical statistics

I. INTRODUCTION

THE goal of structural biology is to determine the 3-D geometry of a biological macromolecular complex. Such complexes, for example, a virus, function as machines and are typically called “particles”. The 3-D geometry, typically called the “structure”, can be as detailed as the 3-D location of each atom in the particle or, if only lower resolution is achievable, the electron density as a function of position in 3-D (in x-ray crystallography) or the electron scattering intensity as a function of position in 3-D (in electron microscopy). Understanding the 3-D geometry of synthetic nanoparticles is also becoming important in materials science [1]–[3]. Structural biology has long been dominated by x-ray crystallography which has very limited capability for dealing with heterogeneity and dynamics among the particles. In particular, the particles making up the crystal must be sufficiently uniform to allow the formation of a crystal and then the additional non-biological interactions between neighboring particles in the crystal further restrict the individual particles. Finally the data is a function of the entire crystal, i.e., a function of all of the particles. Therefore x-ray crystallography provides a 3-D snapshot of a particular state of the particle rather than

following a single instance of the particle through the 4-D trajectory that it would experience in its natural environment.

Single-particle cryo electron microscopy (cryo EM) is transforming structural biology [4] because, due to better image detectors [5], phase plates [6] for improved image contrast, and more sophisticated statistical computing [7]–[9], cryo EM is beginning to provide atomic-resolution structures similar to those of x-ray crystallography without the need to create a crystal. This is a very important advance because many particles simply do not form crystals for a variety of biophysical reasons. However, more important for understanding the functioning of the particles, cryo EM has the capability of displaying heterogeneity and dynamics among the particles.

In a cryo EM experiment, typically 10^4 – 10^6 noisy 2-D projection images of the 3-D electron scattering intensity of the flash-frozen particles are recorded, one image for each instance of the particle. Typical particle weights are in the range of 10^5 – 10^8 Daltons. The experimental design is dominated by the desire to avoid damage to the particle by the electron beam. In particular, damage minimization is achieved by low dose (leading to noisy images), by recording only one projection image per particle (unlike medical x-ray computed tomography), and by performing the experiment on flash-frozen particles at cryogenic temperatures. Because the orientation of the particle during the flash freezing is not controlled, the orientation of the projection image is random and because the image is noisy, the projection direction cannot be determined from an individual image alone. Standard computational methods assume that all instances of the particle are identical or that all instances of the particle belong to one of a few discrete classes (“discrete heterogeneity”, the class label for each image is not known, typically there are less than ten classes) and that every instance within a class is identical. Then a structure is computed for each class, possibly at atomic resolution. More sophisticated approaches characterize the continuous heterogeneity of the particles within each class.

The geometric symmetry of the particle is an important aspect of structural studies of both biological and synthetic particles. Many so-called spherical viruses, which include polio virus and other human pathogens, have a so-called capsid that is constructed out of many copies of a peptide building block which are arranged in pattern that has icosahedral symmetry much like a human-made geodesic dome. Symmetry is described mathematically as a rotational point group. This

N. Xu is with the School of Electrical and Computer Engineering, Cornell University, Ithaca, NY, 14853 USA e-mail: nx25@cornell.edu

P.C. Doerschuk is with the School of Electrical and Computer Engineering and the Nancy E. and Peter C. Meinig School of Biomedical Engineering, Cornell University, Ithaca, NY, 14853 USA e-mail: pd83@cornell.edu

paper describes how to impose symmetry on the statistics of the particle rather than on each realization of the particle (Sections II, III, IV, and VII) and how to integrate this mathematical model of the particle into a maximum likelihood reconstruction method (Section V). The result is demonstrated on images of a Virus Like Particle of bacteriophage HK97 (Section VI).

The approach of this paper is focused on the estimation of first and second order statistics of the electron scattering intensity of the particles in order to characterize the heterogeneity of the particles and related work is discussed in Section II. However there are other approaches to characterizing the differences among the particles visualized by cryo EM. Prominent approaches include direct reconstruction of principal components [10], low-dimensional manifold embedding of multiple reconstructions with interpolation to create trajectories [11], [12], and normal modes of a references model [13]. These papers do not concern symmetry (the numerical examples are all ribosome problems) and so are outside of the scope of this paper.

Notation: E denotes expectation, i.i.d. stands for “independent and identically distributed”, $\mathbf{x} \in \mathbb{R}^3$, and $x = \|\mathbf{x}\|_2$. The quantity \mathbf{x}/x is a unit vector and, since $\mathbf{x} \in \mathbb{R}^3$, is shorthand for the two angles of spherical coordinates. I_n is the $n \times n$ identity matrix and $0_{m,n}$ is the $m \times n$ zero matrix. $\int d\Omega$ is integration over the surface of the sphere in 3-D which, in spherical coordinates, is $\int_{\theta=0}^{\pi} \int_{\phi=0}^{2\pi} \sin(\theta) d\theta d\phi$. Define the Kronecker delta function $\delta_{m,n}$ by $\delta_{m,n} = 1$ if $m = n$ and $= 0$ otherwise where m and n are integers or vectors of integers.

II. SYMMETRY AND SYMMETRICAL STATISTICS

The symmetries that are relevant to the cryo EM application are the 3-D rotational point group symmetries which are the icosahedral I , octahedral O , tetrahedral T , cyclic C_n ($n \in \{1, 2, \dots\}$), and dihedral D_n ($n \in \{1, 2, \dots\}$) groups. Once a coordinate system is chosen, each of these groups can be described as a collection of matrices denoted by $R_\beta \in \mathbb{R}^{3 \times 3}$ ($\beta \in \{1, \dots, N_g\}$) which are rotation matrices, i.e., $R_\beta^{-1} = R_\beta^T$ and $\det R_\beta = +1$. The value of N_g is 60, 24, 12, n , and $2n$ for I , O , T , C_n , and D_n , respectively.

The symmetry can be applied in three different ways. (1) Assume that the particles in a class are identical and that the common electron scattering intensity, which is denoted by $\rho(\mathbf{x})$, has the symmetry, i.e., $\rho(R_\beta^{-1}\mathbf{x}) = \rho(\mathbf{x})$ for all $\beta \in \{1, \dots, N_g\}$ and $\mathbf{x} \in \mathbb{R}^3$. This is available in essentially all software systems, e.g., Refs. [7]–[9], [14]–[16]. (2) Assume that each particle in a class is different but that each particle has the symmetry so that the electron scattering intensity of the i th particle, which is denoted by $\rho_i(\mathbf{x})$, satisfies $\rho_i(R_\beta^{-1}\mathbf{x}) = \rho_i(\mathbf{x})$ for all $\beta \in \{1, \dots, N_g\}$ and $\mathbf{x} \in \mathbb{R}^3$. This is available in some software systems by resampling [17]–[21] (implemented, for instance, in Ref. [7]), moment estimators [22]–[24], or maximum likelihood estimation of the parameters of a probabilistic model for the Fourier series coefficients of the electron scattering intensity [25]–[30]. It is known that the resulting spatial variance functions (i.e., the variance as a function of position) have anomalous peaks on

and near symmetry axes of the particle [31, p. 173]. Since the symmetry axes can be the location of important biology, e.g., in Flock House Virus (FHV) [32], [33], the biology concerning the pentamer of γ peptides near the 5-fold symmetry axis of the icosahedrally symmetric particle [34], [35], so anomalous results near symmetry axes is not a satisfactory situation. (3) Assume that each particle in a class is different, that no particle has the symmetry, but the statistics of the i.i.d. ensemble of particles has the symmetry as is described in the following paragraph. The authors are unaware of prior work of this type.

One approach to introduce symmetric statistics is to require symmetry in all of the finite-dimensional probability measures that together, via Kolmogorov’s extension theorem [36, Theorem 2.1.5 p. 11], define the electron scattering intensity stochastic process. If the probability measures can be described by probability density functions (pdfs), then the symmetry condition is $p_{R_\beta^{-1}\mathbf{x}_1, \dots, R_\beta^{-1}\mathbf{x}_k}(\rho_1, \dots, \rho_k) = p_{\mathbf{x}_1, \dots, \mathbf{x}_k}(\rho_1, \dots, \rho_k)$ for all $\beta \in \{1, \dots, N_g\}$, $k \in \{1, 2, \dots\}$, $\mathbf{x}_1, \dots, \mathbf{x}_k \in \mathbb{R}^3$, and $\rho_1, \dots, \rho_k \in \mathbb{R}$. Define the mean function and covariance function of the electron scattering intensity, denoted by $\bar{\rho}(\mathbf{x})$ and $C(\mathbf{x}_1, \mathbf{x}_2)$, respectively, by $\bar{\rho}(\mathbf{x}) = E[\rho(\mathbf{x})]$ and $C(\mathbf{x}_1, \mathbf{x}_2) = E[(\rho(\mathbf{x}_1) - \bar{\rho}(\mathbf{x}_1))(\rho(\mathbf{x}_2) - \bar{\rho}(\mathbf{x}_2))]$, respectively. From the $k = 1$ and $k = 2$ instances of the symmetry condition for the pdfs, it is straightforward to compute that

$$\bar{\rho}(R_\beta^{-1}\mathbf{x}) = \bar{\rho}(\mathbf{x}) \quad (1)$$

$$\text{for any } \mathbf{x} \in \mathbb{R}^3 \text{ and } \beta \in \{1, \dots, N_g\},$$

$$C(R_\beta^{-1}\mathbf{x}_1, R_\beta^{-1}\mathbf{x}_2) = C(\mathbf{x}_1, \mathbf{x}_2) \quad (2)$$

$$\text{for any } \mathbf{x}_1, \mathbf{x}_2 \in \mathbb{R}^3 \text{ and } \beta \in \{1, \dots, N_g\}.$$

If the electron scattering intensity is assumed to be Gaussian, the benefits of which are described in Ref. [25] and outlined in Section V, then Eqs. 1–2 imply that the symmetry condition for the pdfs is satisfied for all values of k .

III. BASIS FUNCTIONS

The particle is described as a linear combination of basis functions, specifically,

$$\rho(\mathbf{x}) = \sum_{\omega} c_{\omega} F_{\omega}(\mathbf{x}), \quad (3)$$

where c_{ω} are random variables and $F_{\omega}(\mathbf{x})$ are known functions. The goal of the reconstruction calculation (Section V) is to estimate the joint probability distribution of the c_{ω} . To achieve the desired constraints on the first and second order statistics of $\rho(\mathbf{x})$ (Eqs. 1 and 2) requires constraints on the first and second order statistics of c_{ω} . Determining these constraints is simplified if $F_{\omega}(\mathbf{x})$ have specific properties under rotations from the symmetry point group of the particle.

The numerical example of Section VI concerns a virus with icosahedral (I) symmetry. For I (and also for O and T), the rotational symmetry axes are oriented in a variety of directions leading to particles that tend to fill their minimum bounding sphere. Therefore the choice of $F_{\omega}(\mathbf{x})$ that is considered in detail uses spherical coordinates and is the product of a so-called

angular function (which depends on the angles of spherical coordinates and is a linear combination of spherical harmonics¹) and a so-called radial function (which depends on the radius of spherical coordinates), i.e., $F_\omega(\mathbf{x}) = I_\omega(\mathbf{x}/x)\psi_\omega(x)$ where $x = \|\mathbf{x}\|_2$ and ω is an index. For C_n and possibly D_n , it is possible to use the same framework but, especially for C_n , it might be more natural to use cylindrical coordinates and a product of a so-called axial function (in z), a polar function (in ϕ), and a radial function (in r). Because rotations of \mathbf{x} do not effect $x = \|\mathbf{x}\|$, in this section we focus on $I_\omega(\mathbf{x}/x)$.

Ref. [38] derives a basis $I_\omega(\mathbf{x}/x)$ that has precise properties under the operations of a rotational point group. In order to describe the properties of the basis, it is necessary to describe the idea of representations. A representation (rep) of a rotational point group, which is a finite group, is a set of matrices which are homomorphic under matrix multiplication to the group elements [39, p. 61]. The irreducible representations (irreps) of a finite group are a set of unitary reps such that all unitary reps can be decomposed into a direct sum of the irreps [39, Theorem 3.3 p. 69]. For the icosahedral and octahedral cases, all irreps can be chosen to be real-valued orthonormal rather than complex-valued unitary and, because of the biological importance of the icosahedral case, the remainder of this section focuses on the real-valued orthonormal icosahedral case. Let N_{rep} be the number of irreps of the N_g -order group G . Let the set of real-valued matrices in the p th irrep be denoted by $\Gamma^p(g) \in \mathbb{R}^{d_p \times d_p}$ for all $g \in G$ where $p \in \{1, \dots, N_{\text{rep}}\}$. For the icosahedral group, $N_{\text{rep}} = 5$, $N_g = 60$, and $d_p = 1, 3, 3, 4, 5$ for $p = 1, 2, 3, 4, 5$, respectively. The basis functions $I_{p,\omega}(\mathbf{x}/x)$ were derived [38] by applying real-valued generalized projection operators constructed from real-valued irreps to real-valued spherical harmonics resulting in the index ω being the ordered pair (l, n) where l indexes the subspace defined by spherical harmonics of order l which contains the basis function and n indexes the different basis functions within the subspace. The basis functions $I_{p;l,n}(\mathbf{x}/x)$ have the properties

- 1) Each $I_{p;l,n}$ is a d_p -dimensional real-valued vector function, i.e., $I_{p;l,n} \in \mathbb{R}^{d_p}$.
- 2) The $I_{p;l,n}$ functions are orthonormal on the surface of the sphere, i.e.,

$$\int I_{p;l,n}(\mathbf{x}/x) I_{p';l',n'}^T(\mathbf{x}/x) d\Omega = \delta_{p,p'} \delta_{l,l'} \delta_{n,n'} I_{d_p} \quad (4)$$

- 3) The subspace of square integrable functions on the surface of the sphere defined by spherical harmonics of index l , contains a set of $I_{p;l,n}$ functions with a total of $2l + 1$ components.
- 4) Each $I_{p;l,n}$ function has a specific transformation property under rotations from the rotational point group [40, p. 20], in particular,

$$I_{p;l,n}(R_g^{-1}\mathbf{x}/x) = (\Gamma^p(g))^T I_{p;l,n}(\mathbf{x}/x) \quad (5)$$

¹Spherical harmonics are denoted by $Y_{l,m}(\theta, \phi)$ where the degree l satisfies $l \in \mathbb{N}$, the order m satisfies $m \in \{-l, \dots, l\}$ and (θ, ϕ) are the angles of spherical coordinates with $0 \leq \theta \leq \pi$ and $0 \leq \phi \leq 2\pi$ [37, Section 14.30, pp. 378–379].

where T is transpose not Hermitian transpose and R_g is the 3×3 rotation matrix corresponding to the g th element of the group.

Examples of $I_{p;j;l,n}$ functions for $l = 15$ are visualized in Figure 1. Note that $p = 1$ exhibits all of the symmetries of an icosahedron.

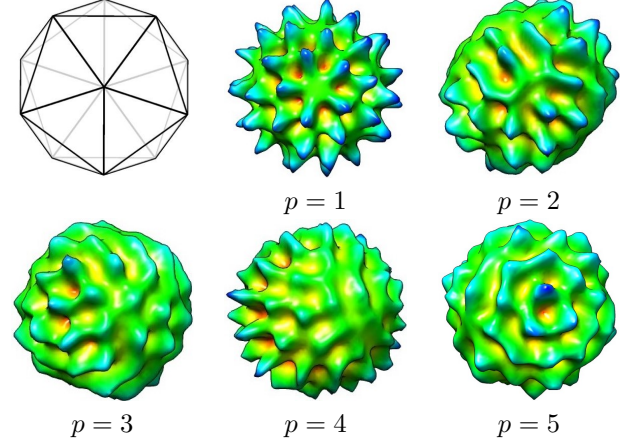


Fig. 1: An icosahedron with a 5-fold axis pointing out of the page and example angular basis functions in the same orientation with $l = 15$ and $p \in \{1, \dots, N_{\text{rep}}\}$. The surfaces of 3-D objects defined by $\xi(\mathbf{x}) = 1$ for $x \leq \kappa_1 + \kappa_2 I_{p;l,n}(\mathbf{x}/x)$ and 0 otherwise, where κ_1 and κ_2 are chosen so that $\kappa_1 + \kappa_2 I_{p;l,n}(\mathbf{x}/x)$ varies between 0.5 and 1.0, are visualized by UCSF Chimera [41] where the color indicates the distance from the center of the object.

IV. CONSTRAINTS ON THE MOMENTS OF THE WEIGHTS CAUSED BY SYMMETRIC STATISTICS

In this section we suppress the index η which describes the class of the particle. The electron scattering intensity, denoted by $\rho(\mathbf{x})$, is described as a linear combination of basis functions where the basis functions are denoted by $I_{p,\zeta}(\mathbf{x}/x)$ (p indexes the irrep, ζ is a shorthand for all other indices, and $x = \|\mathbf{x}\|_2$) and take values in \mathbb{R}^{d_p} (d_p is the dimension of the p th irrep) and the weights in the linear combination are denoted by $c_{p,\zeta}(x)$, also take values in \mathbb{R}^{d_p} , and depend on $x = \|\mathbf{x}\|_2$. In summary,

$$\rho(\mathbf{x}) = \sum_{p=1}^{N_g} \sum_{\zeta} c_{p,\zeta}^T(x) I_{p,\zeta}(\mathbf{x}/x). \quad (6)$$

The electron scattering intensity $\rho(\mathbf{x})$ is real-valued. In this section we deal with the situation where there are a complete set of real-valued orthonormal irreps (including the important icosahedral case) so that $I_{p,\zeta}(\mathbf{x}/x)$ can be taken as real and therefore $c_{p,\zeta}$ can also be taken as real. In Section VII the case where $I_{p,\zeta}(\mathbf{x}/x)$ and $c_{p,\zeta}$ are complex-valued is described.

The constraint on the mean function of $c_{p,\zeta}(x)$ is derived in this paragraph. Define $\bar{\rho}(\mathbf{x}) = \mathbb{E}[\rho(\mathbf{x})] \in \mathbb{R}^1$ and $\bar{c}_{p,\zeta}(x) = \mathbb{E}[c_{p,\zeta}(x)] \in \mathbb{R}^{d_p}$. From Eq. 6,

$$\bar{\rho}(\mathbf{x}) = \sum_{p=1}^{N_g} \sum_{\zeta} \bar{c}_{p,\zeta}^T(x) I_{p,\zeta}(\mathbf{x}/x) \quad (7)$$

and from Eqs. 6 and 5 ($g \in \{1, \dots, N_g\}$)

$$\bar{\rho}(R_g^{-1}\mathbf{x}) = \sum_{p=1}^{N_g} \sum_{\zeta} \bar{c}_{p,\zeta}^T(x) (\Gamma^p(g))^T I_{p,\zeta}(\mathbf{x}/x). \quad (8)$$

From Eq. 1 it follows that the left hand sides of Eqs. 7 and 8 are equal so that for all $g \in \{1, \dots, N_g\}$,

$$\sum_{p=1}^{N_g} \sum_{\zeta} \bar{c}_{p,\zeta}^T(x) [I_{d_p} - (\Gamma^p(g))^T] I_{p,\zeta}(\mathbf{x}/x) = 0. \quad (9)$$

Multiplying by $I_{p',\zeta'}^T(\mathbf{x}/x)$ and integrating over the surface of the sphere implies [via the orthogonality of the $I_{p,\zeta}(\mathbf{x}/x)$ functions (Eq. 4)] that for all $g \in \{1, \dots, N_g\}$,

$$\bar{c}_{p',\zeta'}^T(x) [I_{d_{p'}} - (\Gamma^{p'}(g))^T] = 0_{1,d_{p'}}. \quad (10)$$

Taking transposes and renaming p' to p and ζ' to ζ gives that for all $g \in \{1, \dots, N_g\}$,

$$[I_{d_p} - \Gamma^p(g)] \bar{c}_{p,\zeta}(x) = 0_{d_p,1}. \quad (11)$$

The identity irrep is the $p = 1$ case and for this case, $d_{p=1} = 1$ and $\Gamma^{p=1}(g) = 1$ for all $g \in \{1, \dots, N_g\}$ so that $\bar{c}_{p=1,\zeta}(x)$ is unconstrained by Eq. 11. Eq. 11 implies that for all $g \in \{1, \dots, N_g\}$,

$$\Gamma^p(g) \bar{c}_{p,\zeta}(x) = \bar{c}_{p,\zeta}(x). \quad (12)$$

Consider $p \in \{2, \dots, N_{\text{rep}}\}$ such that $d_p > 1$. If $\bar{c}_{p,\zeta}(x) \neq 0_{d_p,1}$ then there is at least a one-dimensional subspace which is invariant under the action of $\Gamma^p(g)$ for all $g \in \{1, \dots, N_g\}$ and therefore, by definition [39, p. 67], $\Gamma^p(g)$ is not an irrep. But this contradicts the assumption that $\Gamma^p(g)$ is an irrep. Therefore, the statement $\bar{c}_{p,\zeta}(x) \neq 0_{d_p,1}$ must be false. Finally, consider $p \in \{2, \dots, N_{\text{rep}}\}$ such that $d_p = 1$. If $\bar{c}_{p,\zeta}(x) \neq 0$ then Eq. 12 implies that $\Gamma^p(g) = 1$ for all $g \in \{1, \dots, N_g\}$ but this is the identity irrep which is the $p = 1$ irrep. Therefore, $\bar{c}_{p,\zeta}(x) = 0$. In summary,

$$\bar{c}_{p,\zeta}(x) = \begin{cases} 0_{d_p,1}, & p \in \{2, \dots, N_g\} \\ \text{arbitrary}, & p \in \{1\} \end{cases}. \quad (13)$$

The constraint on the covariance function of $c_{p,\zeta}(x)$ is derived in this paragraph acting as if $c_{p,\zeta}(x)$, $I_{p,\zeta}(\mathbf{x}/x)$, and $\Gamma^p(g)$ are complex valued which simplifies the presentation in Section VII. Define $\tilde{\rho}(\mathbf{x}) = \rho(\mathbf{x}) - \bar{\rho}(\mathbf{x})$ and $\tilde{c}_{p,\zeta}(x) = c_{p,\zeta}(x) - \bar{c}_{p,\zeta}$. Define $C(\mathbf{x}_1, \mathbf{x}_2) = \mathbb{E}[(\rho(\mathbf{x}_1) - \bar{\rho}(\mathbf{x}_1))(\rho(\mathbf{x}_2) - \bar{\rho}(\mathbf{x}_2))] = \mathbb{E}[\tilde{\rho}(\mathbf{x}_1)\tilde{\rho}(\mathbf{x}_2)] \in \mathbb{C}^1$ (as in Section II) and $C_{p_1,\zeta_1;p_2,\zeta_2}(x_1, x_2) = \mathbb{E}[(c_{p_1,\zeta_1}(x_1) - \bar{c}_{p_1,\zeta_1}(x_1))(c_{p_2,\zeta_2}(x_2) - \bar{c}_{p_2,\zeta_2}(x_2))^T] = \mathbb{E}[\tilde{c}_{p_1,\zeta_1}(x_1)\tilde{c}_{p_2,\zeta_2}^T(x_2)] \in \mathbb{C}^{d_{p_1} \times d_{p_2}}$. Eq. 6 implies that

$$\tilde{\rho}(\mathbf{x}) = \sum_{p=1}^{N_g} \sum_{\zeta} \tilde{c}_{p,\zeta}^T(x) I_{p,\zeta}(\mathbf{x}/x) \quad (14)$$

$$= \sum_{p=1}^{N_g} \sum_{\zeta} I_{p,\zeta}^T(\mathbf{x}/x) \tilde{c}_{p,\zeta}(x). \quad (15)$$

From Eq. 15 it follows that

$$C(\mathbf{x}_1, \mathbf{x}_2) = \sum_{p_1=1}^{N_{\text{rep}}} \sum_{\zeta_1} \sum_{p_2=1}^{N_{\text{rep}}} \sum_{\zeta_2} I_{p_1,\zeta_1}^T(\mathbf{x}_1/x_1) \times C_{p_1,\zeta_1;p_2,\zeta_2}(x_1, x_2) I_{p_2,\zeta_2}(\mathbf{x}_2/x_2). \quad (16)$$

and from Eqs. 15 and 5 ($g \in \{1, \dots, N_g\}$)

$$C(R_g^{-1}\mathbf{x}_1, R_g^{-1}\mathbf{x}_2) = \sum_{p_1=1}^{N_{\text{rep}}} \sum_{\zeta_1} \sum_{p_2=1}^{N_{\text{rep}}} \sum_{\zeta_2} I_{p_1,\zeta_1}^T(\mathbf{x}_1/x_1) \times \Gamma^{p_1}(g) C_{p_1,\zeta_1;p_2,\zeta_2}(x_1, x_2) [\Gamma^{p_2}(g)]^T I_{p_2,\zeta_2}(\mathbf{x}_2/x_2). \quad (17)$$

From Eq. 1 it follows that the left hand sides of Eqs. 16 and 17 are equal so that for all $g \in \{1, \dots, N_g\}$,

$$\sum_{p_1=1}^{N_{\text{rep}}} \sum_{\zeta_1} \sum_{p_2=1}^{N_{\text{rep}}} \sum_{\zeta_2} I_{p_1,\zeta_1}^T(\mathbf{x}_1/x_1) \left[C_{p_1,\zeta_1;p_2,\zeta_2}(x_1, x_2) - \Gamma^{p_1}(g) C_{p_1,\zeta_1;p_2,\zeta_2}(x_1, x_2) [\Gamma^{p_2}(g)]^T \right] I_{p_2,\zeta_2}(\mathbf{x}_2/x_2) = 0. \quad (18)$$

Multiplying on the left by $I_{p'_1,\zeta'_1}^*(\mathbf{x}_1/x_1)$ and on the right by $I_{p'_2,\zeta'_2}^H(\mathbf{x}_2/x_2)$ and integrating over the surface of the sphere for both \mathbf{x}_1 and \mathbf{x}_2 implies [via the orthogonality of the $I_{p,\zeta}(\mathbf{x}/x)$ functions (Eq. 4 with $I_{p',l',n'}^T(\mathbf{x}/x)$ replaced by $I_{p',l',n'}^H(\mathbf{x}/x)$] that for all $g \in \{1, \dots, N_g\}$,

$$C_{p'_1,\zeta'_1;p'_2,\zeta'_2}(x_1, x_2) = \Gamma^{p'_1}(g) C_{p'_1,\zeta'_1;p'_2,\zeta'_2}(x_1, x_2) [\Gamma^{p'_2}(g)]^T. \quad (19)$$

Renaming p'_1, ζ'_1, p'_2 , and ζ'_2 to p_1, ζ_1, p_2 , and ζ_2 , respectively, multiplying on the right by $[\Gamma^{p_2}(g)]^*$, taking advantage of the unitarity of the irrep matrices $\Gamma^p(g)$, and moving the second term to the right hand side of the equation gives

$$C_{p_1,\zeta_1;p_2,\zeta_2}(x_1, x_2) [\Gamma^{p_2}(g)]^* = \Gamma^{p_1}(g) C_{p_1,\zeta_1;p_2,\zeta_2}(x_1, x_2) \quad (20)$$

which must be true for all $g \in \{1, \dots, N_g\}$, $p_1, p_2 \in \{1, \dots, N_{\text{rep}}\}$, ζ_1, ζ_2 in their unspecified range, and $x_1, x_2 \in \mathbb{R}^+ \cup \{0\}$. Finally, use the fact that the irreps $\Gamma^p(g)$ ($p \in \{1, \dots, N_{\text{rep}}\}$, $g \in \{1, \dots, N_g\}$) are real-valued orthonormal rather than complex-valued unitary to get

$$C_{p_1,\zeta_1;p_2,\zeta_2}(x_1, x_2) \Gamma^{p_2}(g) = \Gamma^{p_1}(g) C_{p_1,\zeta_1;p_2,\zeta_2}(x_1, x_2) \quad (21)$$

which must be true for all $g \in \{1, \dots, N_g\}$, $p_1, p_2 \in \{1, \dots, N_{\text{rep}}\}$, ζ_1, ζ_2 in their unspecified range, and $x_1, x_2 \in \mathbb{R}^+ \cup \{0\}$. This set of matrix equations each of dimension $d_{p_1} \times d_{p_2}$ has substantial structure because the $\Gamma^p(g)$ ($p_1, p_2 \in \{1, \dots, N_{\text{rep}}\}$, $g \in \{1, \dots, N_g\}$) matrices are irreps that are distinct for $p_1 \neq p_2$. Schur's Lemma [39, Corollary 3.2, p. 70] implies that

$$C_{p_1,\zeta_1;p_2,\zeta_2}(x_1, x_2) = \begin{cases} c_{p_1}(\zeta_1, x_1; \zeta_2, x_2) I_{d_{p_1}}, & p_1 = p_2 \\ 0_{d_{p_1}, d_{p_2}}, & \text{otherwise} \end{cases} \quad (22)$$

where $c_{p_1}(\zeta_1, x_1; \zeta_2, x_2) \in \mathbb{C}$.

The results for the mean function and covariance function of $c_{p,\zeta}(x) \in \mathbb{R}^{d_p}$ given in Eqs. 13 and 22 are infinite-dimensional results. To reduce these to finite-dimensional results for computation, we assume that $c_{p,\zeta}(x)$ is described as

a linear combination of scalar real-valued orthonormal basis functions with vector real-valued weights. In particular,

$$c_{p,\zeta}(x) = \sum_{q=1}^{N_q} c_{p,\zeta,q} \psi_{p,\zeta,q}(x) \quad (23)$$

where $c_{p,\zeta,q} \in \mathbb{R}^{d_p}$, $\psi_{p,\zeta,q}(x) \in \mathbb{R}$, and $\int_{x=0}^{\infty} \psi_{p,\zeta,q_1}(x) \psi_{p,\zeta,q_2}(x) x^2 dx = \delta_{q_1,q_2}$. The goal is to determine the constraints on the mean vector $\bar{c}_{p,\zeta,q}$ and covariance matrix $V_{p_1,\zeta_1,q_1;p_2,\zeta_2,q_2}$ of the weights $c_{p,\zeta,q}$ where $\bar{c}_{p,\zeta,q} = \mathbb{E}[c_{p,\zeta,q}]$ and $V_{p_1,\zeta_1,q_1;p_2,\zeta_2,q_2} = \mathbb{E}[(c_{p_1,\zeta_1,q_1} - \bar{c}_{p_1,\zeta_1,q_1})(c_{p_2,\zeta_2,q_2} - \bar{c}_{p_2,\zeta_2,q_2})^T]$. In this notation,

$$\bar{c}_{p,\zeta}(x) = \sum_{q=1}^{N_q} \bar{c}_{p,\zeta,q} \psi_{p,\zeta,q}(x). \quad (24)$$

To determine the mean vector $\bar{c}_{p,\zeta,q}$, substitute Eq. 24 into Eq. 13, multiply by $\psi_{p,\zeta,q'}(x)x^2$, integrate over $x \in [0, \infty)$, and rename q' to q to find that

$$\bar{c}_{p,\zeta,q} = 0_{d_p,1} \text{ for all } p \in \{2, \dots, N_g\}. \quad (25)$$

To determine the covariance matrix $V_{p_1,\zeta_1,q_1;p_2,\zeta_2,q_2}$, first note from the definition $C_{p_1,\zeta_1;p_2,\zeta_2}(x_1, x_2) = \mathbb{E}[(c_{p_1,\zeta_1}(x_1) - \bar{c}_{p_1,\zeta_1}(x_1))(c_{p_2,\zeta_2}(x_2) - \bar{c}_{p_2,\zeta_2}(x_2))^T]$ that (via Eqs. 23 and 24)

$$C_{p_1,\zeta_1;p_2,\zeta_2}(x_1, x_2) = \sum_{q_1=1}^{N_q} \sum_{q_2=1}^{N_q} \psi_{p_1,\zeta_1,q_1}(x_1) \times V_{p_1,\zeta_1,q_1;p_2,\zeta_2,q_2} \psi_{p_2,\zeta_2,q_2}(x_2), \quad (26)$$

so that

$$V_{p_1,\zeta_1,q'_1;p_2,\zeta_2,q'_2} = \int_{x_1=0}^{\infty} \int_{x_2=0}^{\infty} \psi_{p_1,\zeta_1,q'_1}(x_1) \times C_{p_1,\zeta_1;p_2,\zeta_2}(x_1, x_2) \psi_{p_2,\zeta_2,q'_2}(x_2) x_1^2 x_2^2 dx_1 dx_2. \quad (27)$$

Define $v_{p_1}(\zeta_1, q_1; \zeta_2, q_2) \in \mathbb{R}$ by

$$v_{p_1}(\zeta_1, q_1; \zeta_2, q_2) = \int_{x_1=0}^{\infty} \int_{x_2=0}^{\infty} \psi_{p_1,\zeta_1,q_1}(x_1) \times c_{p_1}(\zeta_1, x_1; \zeta_2, x_2) \psi_{p_2,\zeta_2,q_2}(x_2) x_1^2 x_2^2 dx_1 dx_2. \quad (28)$$

Substitute Eq. 22 into the right hand side of Eq. 27 and then replace q'_1 and q'_2 by q_1 and q_2 , respectively, to find that

$$V_{p_1,\zeta_1,q_1;p_2,\zeta_2,q_2} = \begin{cases} v_{p_1}(\zeta_1, q_1; \zeta_2, q_2) I_{d_{p_1}}, & p_1 = p_2 \\ 0_{d_{p_1}, d_{p_2}}, & \text{otherwise} \end{cases}. \quad (29)$$

The goal of this paper is to estimate $\bar{c}_{p,\zeta,q}$ and $V_{p_1,\zeta_1,q_1;p_2,\zeta_2,q_2}$ or equivalently $v_{p_1}(\zeta_1, q_1; \zeta_2, q_2)$ from image data.

Eq. 29 implies structure for the complete covariance matrix V . Suppose that the basis functions are enumerated with indices changing in the order p (slowest), ζ , q , and j (fastest) where j is the index that enumerates the elements of the vector $I_{p,\zeta}(\mathbf{x}/x)$. Then the V matrix is a block matrix with $N_{\text{rep}} \times N_{\text{rep}}$ blocks (determined by the values of the p indices) and only the diagonal blocks are nonzero (due to the “ $p_1 = p_2$ ” condition in Eq. 29). Furthermore, each block is constructed of $N_{\zeta,q} \times N_{\zeta,q}$ subblocks (where $N_{\zeta,q}$ is the total number of (ζ, q) pairs) and each subblock is proportional to the $d_p \times d_p$ identity matrix with proportionality constant $v_{p_1}(\zeta_1, q_1; \zeta_2, q_2)$.

V. HETEROGENEOUS RECONSTRUCTION WITH SYMMETRICAL STATISTICS

This section describes the maximum likelihood estimator that computes the first and second order statistics of the weights in the orthonormal expansion of the electron scattering intensity $\rho(\mathbf{x})$ from the image data under the constraint of symmetrical statistics for $\rho(\mathbf{x})$ (Eqs. 1 and 2).

The standard imaging model is that the 2-D image is the projection along the axis of the microscope of the 3-D electron scattering intensity of the particle linearly modified by the so-called contrast transfer function of the microscope and observed with an unknown translation in additive noise. Let N_v be the number of 2-D projection images. For the i th particle and i th image, let \mathbf{c}_i be the random variable coefficients in the orthonormal expansion for $\rho_i(\mathbf{x})$. Since $\rho_i(\mathbf{x})$ is a linear function of \mathbf{c}_i and the standard imaging model is a linear function of $\rho_i(\mathbf{x})$, there is a linear relationship between the i th image and \mathbf{c}_i , which can be written in the spatial frequency domain (so-called reciprocal space) by the projection slice theorem. Specifically [25],

$$\mathbf{y}_i = L(z_i) \mathbf{c}_i + \mathbf{w}_i \quad (30)$$

where \mathbf{y}_i is the i th 2-D projection image in reciprocal space, z_i is a vector of nuisance parameters which include the projection orientation of the i th image and the projected location of the particle in the i th image, $\mathbf{c}_i \in \mathbb{R}^{N_c}$ is the vector of weights of the i th image, $L(z_i)$ is the transformation matrix from weights to the i th reciprocal-space image, and \mathbf{w}_i is the noise which corrupts the i th image. We assume that the noise \mathbf{w}_i and the weights \mathbf{c}_i are jointly Gaussian and independent with pdfs $\mathbf{w}_i \sim N(0, Q)$ and $\mathbf{c}_i \sim N(\bar{\mathbf{c}}, V)$.

A maximum likelihood estimator is used to estimate $\bar{\mathbf{c}}$ and V from the image data, as is described in Ref. [25]. The maximum likelihood estimator is computed by an expectation-maximization algorithm with nuisance parameters $\{z_i\}_{i=1}^{N_v}$. The jointly Gaussian assumption on \mathbf{c}_i and \mathbf{w}_i is quite important because then the stochastic part of \mathbf{c}_i can be combined with \mathbf{w}_i , specifically,

$$\mathbf{y}_i = L(z_i) \bar{\mathbf{c}}_i + \mathbf{w}'_i \quad (31)$$

where $E[\mathbf{w}'_i | z_i] = 0$ and $E[\mathbf{w}_i \mathbf{w}_i^T | z_i] = L(z_i) V L^T(z_i) + Q$. This transformation removes $\{\mathbf{c}_i\}_{i=1}^{N_v}$ from the set of nuisance parameters at the cost of having a noise \mathbf{w}'_i with a structured covariance matrix. Alternating updates of $\bar{\mathbf{c}}$ and V are used. Additional algorithmic results are described in Ref. [25] including results for multiple discrete classes of particle where the *a priori* distribution is to be estimated.

Our previous calculations [25]–[27], [29] were for icosahedral symmetry and used only the $p = 1$ subset of the basis functions described in Section III. By direct calculation or based on the results in Section IV, no constraints on $\bar{\mathbf{c}}$ or V are required in order to achieve Eqs. 1 and 2. The optimization of V uses Matlab’s `fmincon` (option “trust-region-reflective”) with symbolic cost, gradient of the cost, and Hessian of the cost. In order to incorporate the complete set of basis functions (i.e., all values of p) into this software [42], we think of the mean vector and covariance matrix as functions of a further

level of parameterization. The further level of parameterization is quite simple. Specifically, the mean is either arbitrary or zero (Eq. 25) so the further parameters are the arbitrary values while the covariance has certain elements that must be equal but are otherwise arbitrary (Eq. 29) so the further parameters are the arbitrary values. Using the additional level of parameterization, the gradient and Hessian can be computed via the chain rule. These equations compute the necessary gradient and Hessian in terms of larger vectors and matrices which are then reduced in size. While this approach fits the software easily, more efficient approaches may be possible.

VI. RECONSTRUCTION RESULTS

Numerical results on both synthetic and experimental images of a Virus Like Particle (VLP) derived from bacteriophage HK97 [43] are described in this section. The VLP is essentially the bacteriophage minus the bacteriophage's portal, tail, and genome leaving only the icosahedrally symmetric capsid. HK97 has a complicated lifecycle wherein it first self-assembles in near equilibrium conditions and then undergoes a sequence of essentially irreversible maturation transformations which result in a robust particle capable of surviving outside of the host cell. One of the first steps of maturation is the digestion by a virally-encoded protease of the so-called δ domain of the 60×7 copies of the capsid peptide that together make up the capsid of the bacteriophage. The experimental images [44] come from the particle denoted by $\text{Phi}^{\text{Pro+}}$ [29] which contains a protease that is defective so that the particle is trapped in the Prohead I step of maturation. The average outer radius of the capsid is 254\AA .

Both the synthetic and experimental image calculations are performed in two steps. First a homogeneous reconstruction, i.e., a reconstruction in which all particles are assumed to be identical and have icosahedral symmetry, is performed. In terms of Section V, this is the case where $p = 1$, $\mathbf{c}_i = \bar{\mathbf{c}}$, and $V = 0_{N_c, N_c}$ so this algorithm is denoted by *Hetero (zero covar)*. Second, a heterogeneous reconstruction, i.e., a reconstruction in which no particles are the same, is performed using the homogeneous reconstruction $\bar{\mathbf{c}}$ as an initial condition. Two types of heterogeneous reconstruction are computed and contrasted, one uses only the $p = 1$ basis functions (*Hetero (SymPart)*) so that each particle has the icosahedral symmetry while the other uses the full set of $p \in \{1, \dots, N_{\text{rep}} = 5\}$ basis functions with the constraints of Section IV (*Hetero (SymStat)*) so that no particle has the icosahedral symmetry but the first and second order statistics of the electron scattering intensity $\rho(\mathbf{x})$ do have the icosahedral symmetry. The *Hetero (zero covar)* followed by *Hetero (SymPart)* reconstructions used basis functions with $p = 1$, $l \leq 55$, and $q \leq 20$ (1060 total basis functions) while the *Hetero (zero covar)* followed by *Hetero (SymStat)* reconstructions used $p \in \{1, \dots, N_{\text{rep}}\}$, $l \leq 10$, and $q \leq 20$ (2020 total basis functions) where only smaller l values can be used because of the substantially larger number of basis functions that occur when $p \in \{1, \dots, N_{\text{rep}}\}$ versus $p = 1$. Only diagonal V matrices are considered.

A standard measure of performance in cryo EM is the Fourier shell correlation (FSC) ([45, Eq. 2], [46, Eq. 17],

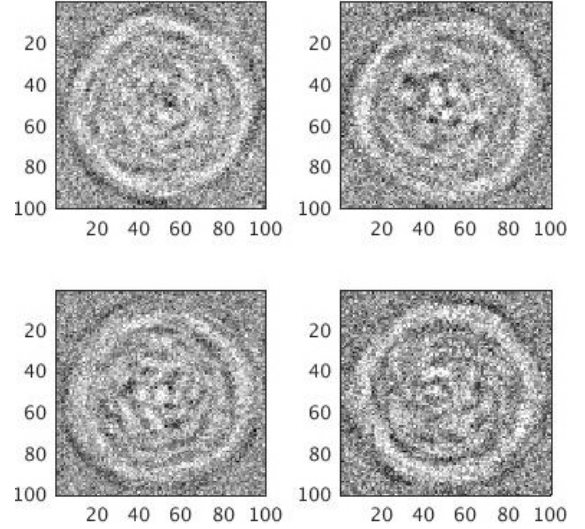


Fig. 2: Four simulated real-space 2-D images of HK97. The color map includes only the lower 98% of the pixel values and saturates on the upper 2%.

[47, p. 879]) between two structures (the two estimates of mean electron scattering intensity) computed from disjoint sets of images. This measure is applied in all calculations, evaluated by the formulas of Ref. [48, Eqs. 22–25]: $\text{FSC}(k) = S_{P_1, P_2}(k) / \sqrt{S_{P_1, P_1}(k) S_{P_2, P_2}(k)}$ where $S_{P_1, P_2}(k) = \int P_1(\mathbf{k}) P_2^*(\mathbf{k}) d\Omega'$ and the integral can be done symbolically [48, Eqs. 23].

A. Simulated images

Simulated 2-D projection images directly in reciprocal space were generated from Eq. 30 which is the mathematical model used in the reconstruction algorithm. There are multiple possible sources for $\bar{\mathbf{c}}$, including from atomic resolution coordinates from x-ray crystallography experiments, but few sources for V . The values of $\bar{\mathbf{c}}$ and V used in the simulation (“ground truth”) come from the *Hetero (SymStat)* reconstruction results. Each of the 1200 images measures 100×100 pixels with a pixel sampling interval of 5.52\AA and a SNR of 0.5 measured on variance not standard deviation. Examples of the simulated real-space 2-D images are shown in Fig. 2.

The sampling interval is 5.52\AA so the Nyquist spatial frequency for the images is $0.5/5.52 = 0.0906\text{\AA}^{-1}$. Over this range the FSC curve based on reconstructions from the non-overlapping subsets of images is very close to 1 so that the structures are essentially identical. Due to computation limits imposed by our computer system, the number of basis functions that can be used is limited which restricts the spatial resolution that can be achieved. One measure of this restriction is that the spherically averaged energy (the denominator of FSC) is quite small by $k = 0.0906\text{\AA}^{-1}$, approximately 10^{-6} times its peak value.

B. Experimental images

Limitations of our computer system make it impossible to process the entire set of images in Ref. [44] so two non-overlapping sets of 1200 images each showing one instance of

the particle were randomly selected for processing. Each image measures 200×200 pixels with a pixel sampling interval of 2.76\AA .

From the mean vector $\bar{\mathbf{c}}$ and the covariance matrix V , it is possible to compute the mean function $\bar{\rho}(\mathbf{x}) = E[\rho(\mathbf{x})]$ (Eqs. 7 and 24 or Ref. [25, Eq. 16]), and covariance function $C(\mathbf{x}_1, \mathbf{x}_2) = E[(\rho(\mathbf{x}_1) - \bar{\rho}(\mathbf{x}_1))(\rho(\mathbf{x}_2) - \bar{\rho}(\mathbf{x}_2))]$ (Eqs. 16 and 26 or Ref. [25, Eq. 18]) of the electron scattering intensity $\rho(\mathbf{x})$ of the particle. We often visualize $s_\rho(\mathbf{x}) = \sqrt{C(\mathbf{x}, \mathbf{x})}$ which has the same units as $\bar{\rho}(\mathbf{x})$ and is only 3-D versus 6-D. Two pairs of mean function $\bar{\rho}(\mathbf{x})$ and standard deviation function $s_\rho(\mathbf{x})$ were computed based on the estimates provided by Hetero (*SymPart*) and Hetero (*SymStat*). The two pairs were computed twice based on the different non-overlapping subsets of the images.

FSC was computed for the Hetero (*SymPart*) reconstructions from the non-overlapping subsets of images with the result that resolution is 0.061\AA^{-1} (equivalently 16.4\AA) based on the frequency at which the FSC curve crosses the 0.5 level. The same calculation for the Hetero (*SymStat*) reconstruction leads to an FSC curve that is almost 1 for the entire range of frequencies out to the Nyquist frequency for the images which is $0.5/2.76 = 0.181\text{\AA}^{-1}$ since the pixel sampling interval is 2.76\AA . Therefore these two structures are essentially identical.

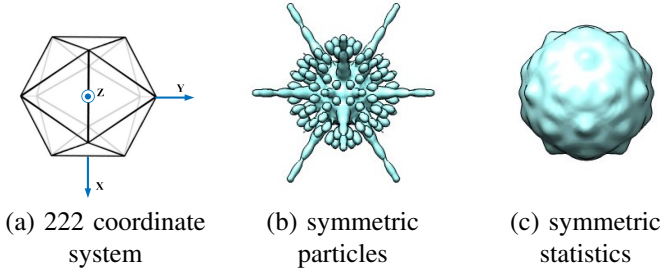


Fig. 3: 3-D reconstructions of the standard deviation $s_\rho(\mathbf{x})$ for $\text{PhI}^{\text{Pro+}}$. The shape is a surface of constant intensity (0.0038) of the standard deviation $s_\rho(\mathbf{x})$, which is visualized by UCSF Chimera [41]. The panel “symmetric particles” (“symmetric statistics”) is computed by Hetero (*SymPart*) (Hetero (*SymStat*)).

Figs. 3(b) and (c) show the standard deviation $s_\rho(\mathbf{x})$ computed by Hetero (*SymPart*) and Hetero (*SymStat*), respectively. In Fig. 4, $\bar{\rho}(\mathbf{x})$ computed by Hetero (*SymPart*) and the two heterogeneous solutions $s_\rho(\mathbf{x})$ computed by Hetero (*SymPart*) and Hetero (*SymStat*) are jointly visualized by computing a 3-D surface of constant value of $\bar{\rho}(\mathbf{x})$ and coloring the surface by $s_\rho(\mathbf{x})$. The $\bar{\rho}$ and s_ρ functions in Figs. 3–4 have the same orientation as is shown in Fig. 3(a), wherein the x-, y-, and z-axes are all 2-fold rotational symmetry axes of the icosahedron which is one of two possible so-called 222 coordinate systems. Fig. 5 shows cross sections of the standard deviation function $s_\rho(\mathbf{x})$ with contours of the mean function $\bar{\rho}(\mathbf{x})$. Each cross section is either perpendicular to one of the three types of symmetry axis (5-, 3-, and 2-fold) or includes the symmetry axis as is described in the diagrams in the upper

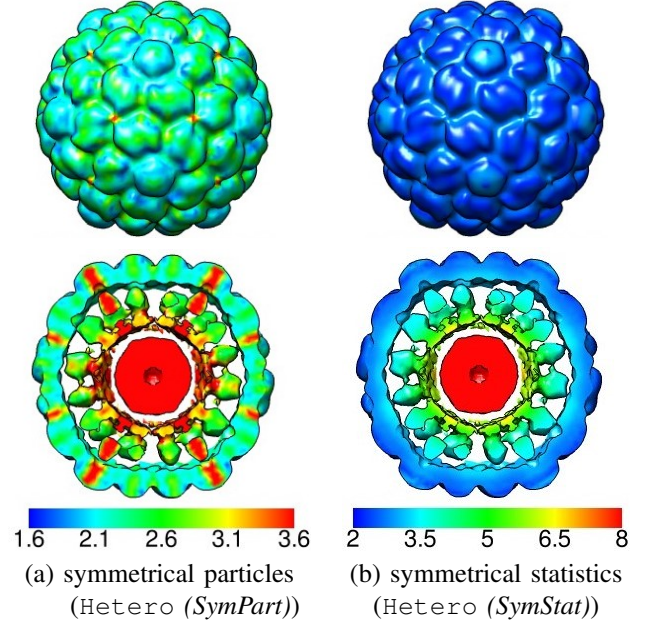


Fig. 4: 3-D reconstructions of $\bar{\rho}$ for $\text{PhI}^{\text{Pro+}}$ from Hetero (*SymPart*) and Hetero (*SymStat*) displayed with different colormaps. The shape is a surface of constant intensity (5×10^{-4}) of $\bar{\rho}(\mathbf{x})$ colored by the standard deviation $s_\rho(\mathbf{x})$, which is visualized by UCSF Chimera [41]. All markings are scaled by 10^{-3} .

row. Results are shown for both a Hetero (*SymPart*) and a Hetero (*SymStat*) reconstruction.

The primary conclusion from Figs. 3–5 is that the assumption of symmetrical particles (i.e., Hetero (*SymPart*)) leads to unphysical peaks in the variance $s_\rho(\mathbf{x})$ near and on symmetry axes while these peaks are not present when using the assumption of symmetrical statistics (i.e., Hetero (*SymStat*)). Using a different approach, specifically, a resampling approach, but still assuming that each particle is symmetric, this same type of artifact is well-known to be a common result [31, p. 173] from standard software systems, e.g., EMAN2 [7]. The radially-directed artifacts in Figs. 3–5 are inconsistent with the annularly structured $\text{PhI}^{\text{Pro+}}$ particle, which has, from outside to inside, annuli of well ordered capsid protein, poorly order capsid δ domain and protease protein, and poorly ordered DNA genome. The annular characteristic of the standard deviation function $s_\rho(\mathbf{x})$ from the Hetero (*SymStat*) reconstruction is particularly clear in Fig. 3(b) and even more so in Fig. 4(a). The annularly-directed artifacts are the origin of the light blue radial lines in Fig. 5(a) while the actual physical structure of the particle is the origin of the annular character of Fig. 5(b). In summary, the results based on assuming symmetric statistics (Hetero (*SymStat*)) rather than symmetric particles (Hetero (*SymPart*)) make more biological sense. Previous analyses based on Hetero (*SymPart*) primarily used the square root of the spherical average of the variance $C(\mathbf{x}, \mathbf{x})$ and therefore the peaks along radially-directed lines were averaged out leading to interpretable information. However, as we try to increase the spatial detail of our interpretation, such behavior is difficult to understand.

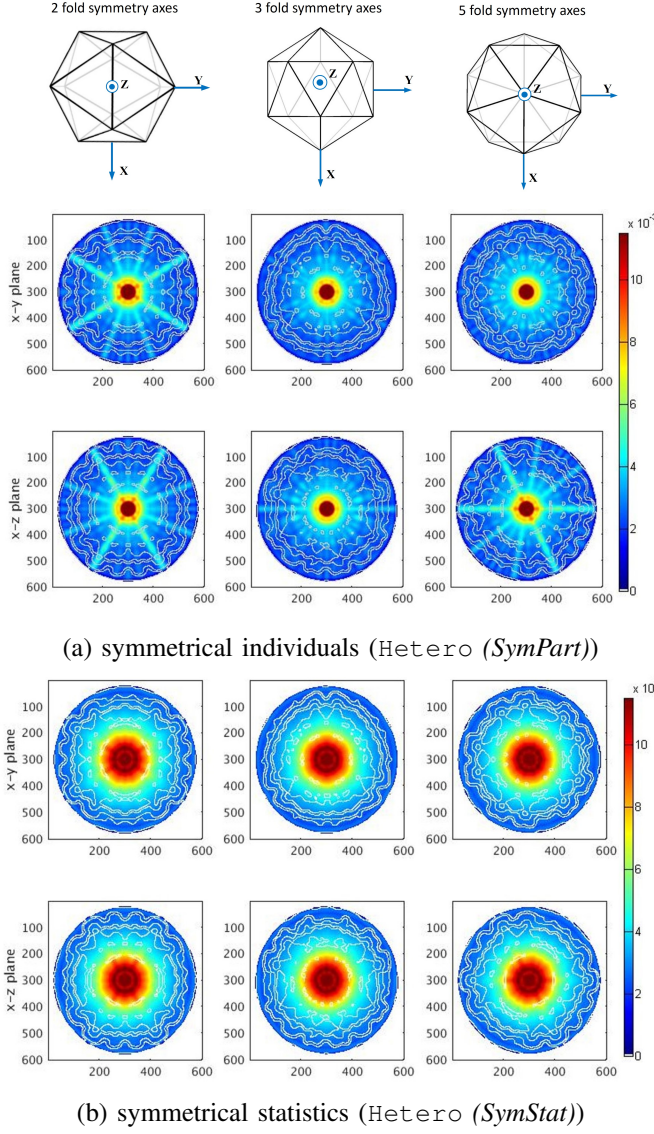


Fig. 5: Cross sections of the standard deviation function $s_\rho(\mathbf{x})$ for $\text{Phi}^{\text{Pro}+}$ using both Hetero (*SymPart*) and Hetero (*SymStat*) and displayed with a common color map. The white lines depict contour levels of the mean $\bar{\rho}(\mathbf{x})$. The geometrical orientation of the $s_\rho(\mathbf{x})$ function is shown in the top row and for each orientation, cross sections in the x - y and x - z planes are displayed so that, for instance, a cross section perpendicular to a 5-fold axis and a cross section that contains a 5-fold axis are both shown. Panel (a) shows the reconstruction results based on symmetrical particles, i.e., Hetero (*SymPart*), whereas Panel (b) shows the reconstruction results based on symmetrical statistics, i.e., Hetero (*SymStat*).

VII. CASES WHERE REAL-VALUED IRREPS ARE NOT AVAILABLE AND NON-SPHERICAL COORDINATE SYSTEMS

Standard references for rotational point group irreps give the irrep matrices in complex-valued unitary form. In some instances, there is no similarity transformation to a real-valued orthonormal form [38]. While it is possible to consider representation theory over a real-valued vector space rather than a complex-valued vector space, the real-valued theory is

more limited [39, p. 70], e.g., a matrix may not have any eigenvalues since the roots of the characteristic polynomial could potentially all be complex. In this section, the constraints on the moments of the weights caused by symmetric statistics are investigated when the irreps and therefore the basis functions and the weights are complex.

The results for the mean function of $c_{p,\zeta}(x)$ are unaltered from Eqs. 7–13.

The results for the covariance function of $c_{p,\zeta}(x)$ are changed from Eqs. 15–20. Because the variables are now complex, it is necessary to compute and to apply symmetry constraints to both $C^{\rho,\rho}(\mathbf{x}_1, \mathbf{x}_2)$ and $C^{\rho,\rho^*}(\mathbf{x}_1, \mathbf{x}_2)$ which are defined by $C^{\rho,\rho}(\mathbf{x}_1, \mathbf{x}_2) = E[(\rho(\mathbf{x}_1) - \bar{\rho}(\mathbf{x}_1))(\rho(\mathbf{x}_2) - \bar{\rho}(\mathbf{x}_2))]$ (the same as $C(\mathbf{x}_1, \mathbf{x}_2)$ in Section IV) and $C^{\rho,\rho^*}(\mathbf{x}_1, \mathbf{x}_2) = E[(\rho(\mathbf{x}_1) - \bar{\rho}(\mathbf{x}_1))(\rho(\mathbf{x}_2) - \bar{\rho}(\mathbf{x}_2))^*]$, respectively. The calculations for $C^{\rho,\rho}$ are the same as Eqs. 15–20. In a more detailed notation where $C_{p_1,\zeta_1;p_2,\zeta_2}^{c,c}(x_1, x_2) = E[(c_{p_1,\zeta_1}(x_1) - \bar{c}_{p_1,\zeta_1}(x_1))(c_{p_2,\zeta_2}(x_2) - \bar{c}_{p_2,\zeta_2}(x_2))^T]$, the result is

$$C_{p_1,\zeta_1;p_2,\zeta_2}^{c,c}(x_1, x_2)[\Gamma^{p_2}(g)]^* = \Gamma^{p_1}(g)C_{p_1,\zeta_1;p_2,\zeta_2}^{c,c}(x_1, x_2). \quad (32)$$

It is not possible to continue on to Eq. 21 because $\Gamma^p(g)$ is no longer real and a new solution is described in the following paragraph. The calculations for C^{ρ,ρ^*} follow the same plan with the result that $[C_{p_1,\zeta_1;p_2,\zeta_2}^{c,c^*}(x_1, x_2) = E[(c_{p_1,\zeta_1}(x_1) - \bar{c}_{p_1,\zeta_1}(x_1))(c_{p_2,\zeta_2}^*(x_2) - \bar{c}_{p_2,\zeta_2}^*(x_2))^T]]$

$$C_{p_1,\zeta_1;p_2,\zeta_2}^{c,c^*}(x_1, x_2)\Gamma^{p_2}(g) = \Gamma^{p_1}(g)C_{p_1,\zeta_1;p_2,\zeta_2}^{c,c^*}(x_1, x_2). \quad (33)$$

Eq. 33 is of the same form as Eq. 21 and so has the same form of solution which is

$$C_{p_1,\zeta_1;p_2,\zeta_2}^{c,c^*}(x_1, x_2) = \begin{cases} c_{p_1}^{c,c^*}(\zeta_1, x_1; \zeta_2, x_2)I_{d_{p_1}}, & p_1 = p_2 \\ 0_{d_{p_1}, d_{p_2}}, & \text{otherwise} \end{cases} \quad (34)$$

The solution to Eq. 32 is described in this paragraph. Two irreps are the same when there exists an invertible matrix S such that $\Gamma_1(g) = S^{-1}\Gamma_2(g)S$ for all g . Since $\Gamma^{p_2}(g)$ is an irrep, it follows that $[\Gamma^{p_2}(g)]^*$ is a rep. By Ref. [39, Theorem 3.5 p. 70], $[\Gamma^{p_2}(g)]^*$ is an irrep. There is a fixed set of irreps, so there must be a function τ from $\{1, \dots, N_{\text{rep}}\}$ to $\{1, \dots, N_{\text{rep}}\}$ such that $[\Gamma^{p_2}(g)]^* = S^{-1}\Gamma^{\tau(p_2)}(g)S$ for some invertible matrix S . The function τ must be a permutation since if $\tau(p_2) = \tau(p'_2) = p_*$ then $S[\Gamma^{p_2}(g)]^*S^{-1} = \Gamma^{p_*}(g)$ and $S'[\Gamma^{p'_2}(g)]^*[S']^{-1} = \Gamma^{p_*}(g)$. Equating the left hand sides of these two equations gives $S[\Gamma^{p_2}(g)]^*S^{-1} = S'[\Gamma^{p'_2}(g)]^*[S']^{-1}$ which implies $T^{-1}\Gamma^{p_2}(g)T = \Gamma^{p'_2}(g)$ (where $T = [S^{-1}S']^*$) which implies that p_2 and p'_2 are the same irrep. Therefore, Eq. 32 is equivalent to

$$C_{p_1,\zeta_1;p_2,\zeta_2}^{c,c}(x_1, x_2)\Gamma^{\tau(p_2)}(g) = \Gamma^{p_1}(g)C_{p_1,\zeta_1;p_2,\zeta_2}^{c,c}(x_1, x_2). \quad (35)$$

Eq. 35 is of the same form as Eq. 21 and so has the same form of solution which is

$$C_{p_1,\zeta_1;p_2,\zeta_2}^{c,c}(x_1, x_2) = \begin{cases} c_{p_1}^{c,c}(\zeta_1, x_1; \zeta_2, x_2)I_{d_{p_1}}, & p_1 = \tau(p_2) \\ 0_{d_{p_1}, d_{\tau(p_2)}}, & \text{otherwise} \end{cases} \quad (36)$$

Rather than $C_{p_1, \zeta_1; p_2, \zeta_2}^{c, c}(x_1, x_2)$ and $C_{p_1, \zeta_1; p_2, \zeta_2}^{c, c^*}(x_1, x_2)$ it is probably more natural to work with the real-valued functions $C_{p_1, \zeta_1; p_2, \zeta_2}^{\Re c, \Re c}(x_1, x_2) = E[\Re[c_{p_1, \zeta_1}(x_1) - \bar{c}_{p_1, \zeta_1}(x_1)]\Re[c_{p_2, \zeta_2}(x_2) - \bar{c}_{p_2, \zeta_2}(x_2)]]^T]$, $C_{p_1, \zeta_1; p_2, \zeta_2}^{\Im c, \Im c}(x_1, x_2) = E[\Im[c_{p_1, \zeta_1}(x_1) - \bar{c}_{p_1, \zeta_1}(x_1)]\Im[c_{p_2, \zeta_2}(x_2) - \bar{c}_{p_2, \zeta_2}(x_2)]]^T]$, and $C_{p_1, \zeta_1; p_2, \zeta_2}^{\Re c, \Im c}(x_1, x_2) = E[\Re[c_{p_1, \zeta_1}(x_1) - \bar{c}_{p_1, \zeta_1}(x_1)]\Im[c_{p_2, \zeta_2}(x_2) - \bar{c}_{p_2, \zeta_2}(x_2)]]^T]$ which can easily be computed via expectations of products of the terms $\Re[c_{p_1, \zeta_1}(x_1) - \bar{c}_{p_1, \zeta_1}(x_1)] = [(c_{p_1, \zeta_1}(x_1) - \bar{c}_{p_1, \zeta_1}(x_1)) + (c_{p_1, \zeta_1}(x_1) - \bar{c}_{p_1, \zeta_1}(x_1))^*]/2$ and $\Im[c_{p_1, \zeta_1}(x_1) - \bar{c}_{p_1, \zeta_1}(x_1)] = [(c_{p_1, \zeta_1}(x_1) - \bar{c}_{p_1, \zeta_1}(x_1)) - (c_{p_1, \zeta_1}(x_1) - \bar{c}_{p_1, \zeta_1}(x_1))^*]/(2i)$. Either $C_{p_1, \zeta_1; p_2, \zeta_2}^{c, c}(x_1, x_2)$ and $C_{p_1, \zeta_1; p_2, \zeta_2}^{c, c^*}(x_1, x_2)$ or $C_{p_1, \zeta_1; p_2, \zeta_2}^{\Re c, \Re c}(x_1, x_2)$, $C_{p_1, \zeta_1; p_2, \zeta_2}^{\Im c, \Im c}(x_1, x_2)$, and $C_{p_1, \zeta_1; p_2, \zeta_2}^{\Re c, \Im c}(x_1, x_2)$ can be made finite-dimensional by the same methods used in Section IV. Finally, after choosing an ordering of the indices (p, ζ) and the real versus imaginary parts, a real-valued positive semi-definite matrix V can be assembled which has block structure similar to the situation in Section IV.

The calculations in this section allow $\rho(\mathbf{x})$ to be complex. However, $\rho(\mathbf{x})$ is real in the cryo EM application. A “penalty function” approach would be to create synthetic measurements of $\Im\rho(\mathbf{x})$ with value 0 and variance σ_{\Im}^2 and process the resulting complex-valued $\rho(\mathbf{x})$, possibly allowing σ_{\Im}^2 to decrease as the iterative algorithm converges. A constraint approach would be to determine additional constraints on $c_{p, \zeta}(x)$ such that $\rho(\mathbf{x})$ is guaranteed to be real. We believe that such constraints involve the behavior of basis functions under conjugation (i.e., for Fourier series with period T in 1-D, $\psi_n^*(t) = [\exp(i2\pi nt/T)]^* = \exp(-i2\pi nt/T) = \psi_{-n}(t)$) and are not closely related to the rotational point-group symmetries discussed in this paper.

Except in this paragraph, results in this paper are stated in the spherical coordinate system (e.g., Eq. 6). Spheres, which are contours of constant radius in spherical coordinates, enclose typical so-called spherical viruses reasonably closely and therefore lead to parsimonious parameterizations. This is typical for particles obeying the symmetries of I , O , and T because the symmetry axes have widely varying directions. However, for particles obeying the symmetries of C_n (and possibly D_n), e.g., the tail of bacteriophage P22 [49], cylindrical coordinates (r, ϕ, z) can be more natural with the single symmetry axis of C_n on the z axis of the coordinate system. For the case of C_n , Eq. 6 is replaced by $\rho(\mathbf{x}) = \sum_{p=1}^{N_g} \sum_{\zeta} c_{p, \zeta}^T(r, z) I_{p, \zeta}(\phi)$ and the constraint of symmetrical statistics specifies the mean and covariance functions of $c_{p, \zeta}(r, z)$ rather than the mean (Eq. 13) and covariance (Eqs. 22, 34, and 36) functions of $c_{p, \zeta}(x)$. The case of D_n is somewhat more complicated because there are additional rotational symmetry axes beyond z axis. In either case, the effect of the symmetrical statistics constraint is a constraint on the covariance function of the coordinate-dependent weights where the weights depend on the coordinates that are not involved in the symmetry operation. Finally, if basis functions $F_{p, \zeta}(\mathbf{x})$ are used which directly have symmetry properties that are the obvious generalization of Eq. 5, then the orthonormal expansion is $\rho(\mathbf{x}) = \sum_{p=1}^{N_g} \sum_{\zeta} c_{p, \zeta}^T F_{p, \zeta}(\mathbf{x})$

with random-variable weights $c_{p, \zeta}$ and there is no mean or covariance function intermediate on the path to mean vector and covariance matrix constraints analogous to Eqs. 25 and 29.

VIII. SYMMETRIZING NON-SYMMETRIC FUNCTIONS

Suppose s is a function from \mathbb{R}^3 to \mathbb{R} . Suppose R_{β} ($\beta \in \{1, \dots, N_g\}$) are the rotation matrices for a point-group symmetry. An important result in theory and software is that

$$\rho(\mathbf{x}) \doteq \sum_{\beta=1}^{N_g} s(R_{\beta}^{-1} \mathbf{x}) \quad (37)$$

has the symmetry described by Eq. 1. The proof is via the Rearrangement Theorem [40, Theorem II, p. 24] which states that a sum over all the elements of a group, i.e., $\sum_{\beta=1}^{N_g} f(R_{\beta})$, is unaltered (although the terms in the sum occur in a permuted order) if R_{β} is replaced by $R_{\beta_0} R_{\beta}$ where β_0 is a fixed element of the group. The purpose of this section is to describe a similar symmetrization procedure for stochastic processes such that the mean (covariance) of the result has the symmetry described by Eq. 1 (Eq. 2).

One construction that leads to a stochastic process with the desired statistics starts with a stochastic process $s(\mathbf{x}) \in \mathbb{R}^{N_g}$ with components $s_i(\mathbf{x})$ that is exchangeable relative to first and second order statistics, i.e., if $s'(\mathbf{x}) \in \mathbb{R}^{N_g}$ is a permutation of the elements of $s(\mathbf{x})$, then $s'(\cdot)$ and $s(\cdot)$ have the same first and second order statistics. This implies that there exist functions $\bar{s}(\mathbf{x})$, $C^=(\mathbf{x}_1, \mathbf{x}_2)$, and $C^{\neq}(\mathbf{x}_1, \mathbf{x}_2)$ such that $\bar{s}_{\beta}(\mathbf{x}) \doteq E[s_{\beta}(\mathbf{x})] = \bar{s}(\mathbf{x})$ (for all $\beta \in \{1, \dots, N_g\}$) and $C_{\beta_1, \beta_2}(\mathbf{x}_1, \mathbf{x}_2) \doteq E[(s_{\beta_1}(\mathbf{x}_1) - \bar{s}(\mathbf{x}_1))(s_{\beta_2}(\mathbf{x}_2) - \bar{s}(\mathbf{x}_2))] = \delta_{\beta_1, \beta_2} C^=(\mathbf{x}_1, \mathbf{x}_2) + (1 - \delta_{\beta_1, \beta_2}) C^{\neq}(\mathbf{x}_1, \mathbf{x}_2)$ (for all $\beta_1, \beta_2 \in \{1, \dots, N_g\}$).

Define $\rho(\cdot)$ by

$$\rho(\mathbf{x}) = \sum_{\beta=1}^{N_g} s_{\beta}(R_{\beta}^{-1} \mathbf{x}). \quad (38)$$

We will directly compute the first and second order statistics of $\rho(\cdot)$ and find that they satisfy Eq. 1 and Eq. 2, respectively, as is desired. For the first order statistics, $\bar{\rho}(\mathbf{x}) \doteq E[\rho(\mathbf{x})] = \sum_{\beta=1}^{N_g} \bar{s}(R_{\beta}^{-1} \mathbf{x})$ which is in the form of Eq. 37 so that $\bar{\rho}(\cdot)$ has the symmetry described by Eq. 1. For the second order statistics,

$$C(\mathbf{x}_1, \mathbf{x}_2) \doteq E[(\rho(\mathbf{x}_1) - \bar{\rho}(\mathbf{x}_1))(\rho(\mathbf{x}_2) - \bar{\rho}(\mathbf{x}_2))] \quad (39)$$

$$= \sum_{\beta_1=1}^{N_g} \sum_{\beta_2=1}^{N_g} C_{\beta_1, \beta_2}(R_{\beta_1}^{-1} \mathbf{x}_1, R_{\beta_2}^{-1} \mathbf{x}_2) \quad (40)$$

$$= \sum_{\beta_1=1}^{N_g} \sum_{\beta_2=1}^{N_g} \left[\delta_{\beta_1, \beta_2} C^=(R_{\beta_1}^{-1} \mathbf{x}_1, R_{\beta_2}^{-1} \mathbf{x}_2) + (1 - \delta_{\beta_1, \beta_2}) C^{\neq}(R_{\beta_1}^{-1} \mathbf{x}_1, R_{\beta_2}^{-1} \mathbf{x}_2) \right]. \quad (41)$$

Independent of the properties of $C^=$ and C^{\neq} , application of the Rearrangement Theorem [40, Theorem II, p. 24] demonstrates the $C(\mathbf{x}_1, \mathbf{x}_2)$ satisfies the symmetry of Eq. 2. For Gaussian stochastic processes, mean and covariance satisfying the constraints of Section IV or VII provides a simulation

method based on the basis functions with special symmetry properties but for non-Gaussian processes, problems with many basis functions having symmetry properties, or problems with basis functions that lack symmetry properties, Eq. 38 provides an alternative method.

IX. CONCLUSION

In this paper we formulate and solve 3-D modeling and reconstruction problems for stochastic signals where the statistics of the stochastic signal are required to have a geometric symmetry. The work is motivated by cryo electron microscopy, which is of great importance in structural biology and of growing importance in the material science of nanoscale particles.

Previous algorithms assumed that the realizations of the stochastic signal have the geometric symmetry. While this implies that the statistics have the symmetry, it is a sufficient condition rather than a necessary condition and it has lead to inaccurate results for the second order statistics of the electron scattering intensity on and near symmetry axes [31, p. 173]. Since these are often locations of important biology, inaccurate results greatly reduce the value of the entire experiment.

Beyond correcting the problem in existing computations, this is the first publication of which the authors are aware in which a full 6-D covariance function is computed. Interpreting the 6-D information is challenging and we are working with our biological collaborators on this problem.

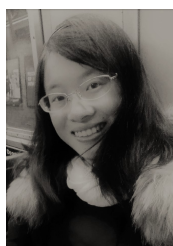
ACKNOWLEDGMENTS

We are grateful to Professors John E. Johnson (The Scripps Research Institute) and David Veesler (University of Washington) for the HK97 data and helpful discussions; to Drs. Yili Zheng and Qiu Wang and to Ms. Yunye Gong for their effort on the Hetero software system; and for support from NSF 1217867.

REFERENCES

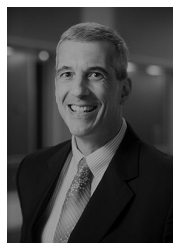
- [1] S. E. Kim, L. Zhang, K. Ma, M. Riegman, F. Chen, I. Ingold, M. Conrad, M. Z. Turker, M. Gao, X. Jiang, S. Monette, M. Pauliah, M. Gonen, P. Zanzonico, T. Quinn, U. Wiesner, M. S. Bradbury, and M. Overholzer, "Ultrasmall nanoparticles induce ferroptosis in nutrient-deprived cancer cells and suppress tumour growth," *Nature Nanotechnology*, vol. 11, no. 11, pp. 977–985, Nov. 2016.
- [2] K. Ma, H. Sai, and U. Wiesner, "Ultrasmall sub-10nm near-infrared fluorescent mesoporous silica nanoparticles," *J. American Chemical Society*, vol. 134, no. 32, pp. 13 180–13 183, 15 Aug 2012.
- [3] Y. He, T. Ye, M. Su, C. Zhang, A. E. Ribbe, W. Jiang, and C. Mao, "Hierarchical self-assembly of DNA into symmetric supramolecular polyhedra," *Nature*, vol. 452, pp. 198–201, 13 March 2008. [Online]. Available: doi:10.1038/nature06597
- [4] S. Subramaniam, W. Kühlbrandt, and R. Henderson, "CryoEM at IUCrJ: a new era," *IUCrJ*, vol. 3, no. 1, pp. 3–7, Jan 2016. [Online]. Available: https://doi.org/10.1107/S2052252515023738
- [5] G. McMullan, A. Faruqi, D. Clare, and R. Henderson, "Comparison of optimal performance at 300 keV of three direct electron detectors for use in low dose electron microscopy," *Ultramicroscopy*, vol. 147, pp. 156 – 163, 2014. [Online]. Available: http://www.sciencedirect.com/science/article/pii/S030439911400151X
- [6] M. Khoshouei, M. Radjainia, A. J. Phillips, J. A. Gerrard, A. K. Mitra, J. M. Plitzko, W. Baumeister, and R. Danev, "Volta phase plate cryo-EM of the small protein complex Prx3," *Nature Communications*, vol. 7, 2016. [Online]. Available: http://dx.doi.org/10.1038/ncomms10534
- [7] G. Tang, L. Peng, P. R. Baldwin, M. D. S., W. Jiang, I. Rees, and S. J. Ludtke, "EMAN2: An extensible image processing suite for electron microscopy," *J. Struct. Biol.*, vol. 157, no. 1, pp. 38–46, 2007.
- [8] S. H. W. Scheres, "RELION: Implementation of a Bayesian approach to cryo-EM structure determination," *J. Struct. Biol.*, vol. 180, pp. 519–530, 2012.
- [9] T. R. Shaikh, H. Gao, W. T. Baxter, F. J. Asturias, N. Boisset, A. Leith, and J. Frank, "Spider image processing for single-particle reconstruction of biological macromolecules from electron micrographs," *Nature Protocols*, vol. 3, no. 12, pp. 1941–1974, 2008.
- [10] H. D. Tagare, A. Kucukelbir, F. J. Sigworth, W. Hongwei, and M. Rao, "Directly reconstructing principal components of heterogeneous particles from cryo-EM images," *J. Struct. Biol.*, vol. 191, pp. 245–262, 2015.
- [11] J. Frank and A. Ourmazd, "Continuous changes in structure mapped by manifold embedding of single-particle data in cryo-EM," *Methods*, vol. 100, pp. 61–67, 2016, single Particle Cryo-EM, from sample to reconstruction. [Online]. Available: http://www.sciencedirect.com/science/article/pii/S1046202316300251
- [12] A. Dashti, P. Schwander, R. Langlois, R. Fung, W. Li, A. Hosseinzadeh, H. Y. Liao, J. Pallesen, G. Sharma, V. A. Stupina, A. E. Simon, J. D. Dinman, J. Frank, and A. Ourmazd, "Trajectories of the ribosome as a brownian nanomachine," *Proceedings of the National Academy of Sciences*, vol. 111, no. 49, pp. 17 492–17 497, 2014. [Online]. Available: http://www.pnas.org/content/111/49/17492.abstract
- [13] Q. Jin, C. O. S. Sorzano, J. M. de la Rosa-Trevín, J. R. Bilbao-Castro, R. Núñez-Ramírez, O. Llorca, F. Tama, and S. Jonić, "Iterative elastic 3D-to-2D alignment method using normal modes for studying structural dynamics of large macromolecular complexes," *Structure*, vol. 22, no. 3, pp. 496–506, 2014. [Online]. Available: http://www.sciencedirect.com/science/article/pii/S0969212614000136
- [14] S. J. Ludtke, P. R. Baldwin, and W. Chiu, "EMAN: semiautomated software for high-resolution single-particle reconstructions," *J. Struct. Biol.*, vol. 128, no. 1, pp. 82–97, Dec. 1 1999.
- [15] S. H. W. Scheres, "A Bayesian view on cryo-EM structure determination," *J. Mol. Biol.*, vol. 415, no. 2, pp. 406–418, 13 January 2012.
- [16] J. Frank, M. Radermacher, P. Penczek, J. Zhu, Y. Li, M. Ladadaj, and A. Leith, "SPIDER and WEB: Processing and visualization of images in 3D electron microscopy and related fields," *J. Struct. Biol.*, vol. 116, pp. 190–199, 1996.
- [17] P. A. Penczek, M. Kimmel, and C. M. T. Spahn, "Identifying conformational states of macromolecules by eigen-analysis of resampled cryo-EM images," *Structure*, vol. 19, pp. 1582–1590, 9 November 2011.
- [18] C. M. T. Spahn and P. A. Penczek, "Exploring conformational modes of macromolecular assemblies by multiparticle cryo-EM," *Current Opinion in Structural Biology*, vol. 19, pp. 623–631, 2009.
- [19] W. Zhang, M. Kimmel, C. M. T. Spahn, and P. A. Penczek, "Heterogeneity of large macromolecular complexes revealed by 3D cryo-EM variance analysis," *Structure*, vol. 16, pp. 1770–1776, 2008.
- [20] P. A. Penczek, C. Yang, J. Frank, and C. M. T. Spahn, "Estimation of variance in single-particle reconstruction using the bootstrap technique," *J. Struct. Biol.*, vol. 154, no. 2, pp. 168–183, 2006.
- [21] A. Simonetti, S. Marzi, A. G. Myasnikov, A. Fabbretti, M. Yusupov, C. O. Gualerzi, and B. P. Klaholz, "Structure of the 30S translation initiation complex," *Nature*, vol. 455, no. 7211, pp. 416–420, 18 Sep. 2008. [Online]. Available: http://dx.doi.org/10.1038/nature07192
- [22] H. Y. Liao, Y. Hashem, and J. Frank, "Efficient estimation of three-dimensional covariance and its application in the analysis of heterogeneous samples in cryo-electron microscopy," *Structure*, vol. 23, no. 6, pp. 1129–1137, 2 June 2015.
- [23] H. Y. Liao and J. Frank, "Classification by bootstrapping in single particle methods," in *Proceedings of the 2010 IEEE International Symposium on Biomedical Imaging*, 14 Apr. 2010, pp. 169–172.
- [24] E. Katsevich, A. Katsevich, and A. Singer, "Covariance matrix estimation for the cryo-EM heterogeneity problem," *SIAM Imaging Science*, vol. 8, no. 1, pp. 126–185, 2015.
- [25] Y. Zheng, Q. Wang, and P. C. Doerschuk, "3-D reconstruction of the statistics of heterogeneous objects from a collection of one projection image of each object," *Journal of the Optical Society of America A*, vol. 29, no. 6, pp. 959–970, Jun. 2012.
- [26] Q. Wang, T. Matsui, T. Domitrovic, Y. Zheng, P. C. Doerschuk, and J. E. Johnson, "Dynamics in cryo EM reconstructions visualized with maximum-likelihood derived variance maps," *Journal of Structural Biology*, vol. 181, no. 3, pp. 195–206, Mar. 2013.
- [27] J. Tang, B. M. Kearney, Q. Wang, P. C. Doerschuk, T. S. Baker, and J. E. Johnson, "Dynamic and geometric analyses of *Nudaurelia capensis* ω virus maturation reveal the energy landscape of particle transitions,"

- Journal of Molecular Recognition*, vol. 27, no. 4, pp. 230–237, 10 February 2014.
- [28] T. Domitrovic, N. Movahed, B. Bothner, T. Matsui, Q. Wang, P. C. Doerschuk, and J. E. Johnson, “Virus assembly and maturation: Auto-regulation through allosteric molecular switches,” *Journal of Molecular Biology*, vol. 425, no. 9, pp. 1488–1496, 13 May 2013.
- [29] Y. Gong, D. Veessler, P. C. Doerschuk, and J. E. Johnson, “Effect of the viral protease on the dynamics of bacteriophage HK97 maturation intermediates characterized by variance analysis of cryo EM particle ensembles,” *Journal of Structural Biology*, vol. 193, no. 3, pp. 188–195, Mar. 2016.
- [30] P. C. Doerschuk, Y. Gong, N. Xu, T. Domitrovic, and J. E. Johnson, “Virus particle dynamics derived from cryoEM studies,” *Current Opinion in Virology*, vol. 18, pp. 57–63, 2016. [Online]. Available: <http://dx.doi.org/10.1016/j.coviro.2016.02.011>
- [31] S. J. Ludtke, “Single-particle refinement and variability analysis in EMAN2.1,” *Methods in Enzymology*, vol. 579, pp. 159–189, 2016, <http://dx.doi.org/10.1016/bs.mie.2016.05.001>.
- [32] A. Odegard, M. Banerjee, and J. E. Johnson, “Flock House Virus: a model system for understanding non-enveloped virus entry and membrane penetration,” *Curr. Top. Microbiol Immunol.*, vol. 343, pp. 1–22, 2010, doi: 10.1007/82_2010_35; PubMed PMID: 20407886.
- [33] H. E. Walukiewicz, M. Banerjee, A. Schneemann, and J. E. Johnson, “Rescue of maturation-defective Flock House Virus infectivity with noninfectious, mature, viruslike particles,” *J. Virol.*, vol. 82, no. 4, pp. 2025–2027, Feb. 2008, pubMed PMID: 18077727; PubMed Central PMCID: PMC2258709.
- [34] A. J. Fisher and J. E. Johnson, “Ordered duplex RNA controls capsid architecture in an icosahedral animal virus,” *Nature*, vol. 361, pp. 176–179, 14 Jan. 1993.
- [35] R. H. Cheng, V. S. Reddy, N. H. Olson, A. J. Fisher, T. S. Baker, and J. E. Johnson, “Functional implications of quasi-equivalence in a $T = 3$ icosahedral animal virus established by cryo-electron microscopy and X-ray crystallography,” *Structure*, vol. 2, no. 4, pp. 271–282, 15 Apr. 1994.
- [36] B. Øksendal, *Stochastic Differential Equations*, 6th ed. Springer-Verlag, 2003.
- [37] F. W. J. Olver, D. W. Lozier, R. F. Boisvert, and C. W. Clark, Eds., *NIST Handbook of Mathematical Functions*. Cambridge, UK: Cambridge University Press, 2010. [Online]. Available: <http://dlmf.nist.gov>
- [38] N. Xu and P. C. Doerschuk, “Computation of real basis functions for the 3-D rotational polyhedral groups T , O , and I ,” *Submitted to SIAM Journal of Mathematical Analysis*, 2017.
- [39] W. Miller, Jr., *Symmetry Groups and Their Applications*. San Deigo: Academic Press, 1972.
- [40] J. F. Cornwell, *Group Theory in Physics*. London: Academic Press, 1984, vol. 1.
- [41] E. F. Pettersen, T. D. Goddard, C. C. Huang, G. S. Couch, D. M. Greenblatt, E. C. Meng, and T. E. Ferrin, “UCSF Chimera—A visualization system for exploratory research and analysis,” *J. Comput. Chem.*, vol. 25, no. 13, pp. 1605–1612, 2004.
- [42] N. Xu and P. C. Doerschuk, “Statistical characterization of ensembles of symmetric virus particles: 3-D stochastic signal reconstruction from electron microscope images,” in *Proceedings of the 38th Annual International Conference of the IEEE Engineering in Medicine and Biology Society (EMBC’16)*. Orlando, FL: IEEE, 17–20 August 2016, pp. 3977–3980, one of 10 finalists in the “EMBS Student Paper Competition” out of more than 2300 papers.
- [43] R. W. Hendrix and J. E. Johnson, “Bacteriophage HK97 capsid assembly and maturation,” *Exp. Med. Biol.*, vol. 726, pp. 351–363, 2012, doi: 10.1007/978-1-4614-0980-9_15.
- [44] D. Veessler, R. Khayat, S. Krishnamurthy, J. Snijder, R. K. Huang, A. J. R. Heck, G. S. Anand, and J. E. Johnson, “Architecture of a dsDNA viral capsid in complex with its maturation protease,” *Structure*, vol. 22, pp. 230–237, 2 February 2014. [Online]. Available: <http://dx.doi.org/10.1016/j.str.2013.11.007>
- [45] M. van Heel, “Similarity measures between images,” *Ultramicroscopy*, vol. 21, pp. 95–100, 1987.
- [46] G. Harauz and M. van Heel, “Exact filters for general geometry three dimensional reconstruction,” *Optik*, vol. 73, no. 4, pp. 146–156, 1986.
- [47] T. S. Baker, N. H. Olson, and S. D. Fuller, “Adding the third dimension to virus life cycles: Three-dimensional reconstruction of icosahedral viruses from cryo-electron micrographs,” *Microbiology and Molecular Biology Reviews*, vol. 63, no. 4, pp. 862–922, Dec. 1999.
- [48] Z. Yin, Y. Zheng, P. C. Doerschuk, P. Natarajan, and J. E. Johnson, “A statistical approach to computer processing of cryo electron microscope images: Virion classification and 3-D reconstruction,” *Journal of Structural Biology*, vol. 144, no. 1/2, pp. 24–50, 2003.
- [49] C. J. Prust, P. C. Doerschuk, G. C. Lander, and J. E. Johnson, “*Ab initio* maximum likelihood reconstruction from cryo electron microscopy images of an infectious virion of the tailed bacteriophage P22 and maximum likelihood versions of Fourier Shell Correlation appropriate for measuring resolution of spherical or cylindrical objects,” *Journal of Structural Biology*, vol. 167, pp. 185–199, 2009.



Nan Xu is pursuing her Ph.D. degree in the School of Electrical and Computer Engineering with a minor in Applied Mathematics and a minor in Cognitive Neuroscience at Cornell University. Nan received her Master of Science degree in May 2015. Before joining Cornell, she received double Bachelor's degrees in Electrical and Computer Engineering (BS) and Mathematics (BA) with a minor in Music at the University of Rochester in Rochester NY. Nan's current research interests are in statistical modeling and inference in biological data. She is investigating

three primary applications: brain network estimation, realistic fMRI data simulation, and reconstruction of the statistical characteristics of ensembles of heterogeneous virus particles.



Peter C. Doerschuk (SM'03) received the B.S., M.S., and Ph.D. degrees in electrical engineering from the Massachusetts Institute of Technology (MIT), Cambridge, in 1977, 1979, and 1985, respectively, and the M.D. degree from Harvard Medical School, Cambridge, MA, in 1987. After postgraduate training at Brigham and Womens' Hospital, he held a postdoctoral appointment with the Laboratory for Information and Decision Systems, MIT, from January 1988 to August 1990. After 16 years on the faculty in Electrical and Computer Engineering,

Purdue University, West Lafayette, IN, he joined the faculty in Biomedical Engineering and Electrical and Computer Engineering, Cornell University, Ithaca, NY, in July 2006.